ADVANCED MATERIALS
www.advmat.de

# Capturing Copper Single Atom in Proton Donor Stimulated O-End Nitrate Reduction

*Yunpeng Zuo, Mingzi Sun, Tingting Li, Libo Sun, Shuhe Han, Yang Chai, Bolong Huang,* and Xin Wang**

**Ammonia ($NH_3$) is vital in global production and energy cycles. Electrocatalytic nitrate reduction (e-$NO_3$RR) offers a promising route for nitrogen (N) conversion and $NH_3$ synthesis, yet it faces challenges like competing reactions and low catalyst activity. This study proposes a synergistic mechanism incorporating a proton donor to mediate O-end e-$NO_3$RR, addressing these limitations. A novel method combining ultraviolet radiation reduction, confined synthesis, and microwave treatment was developed to create a model catalyst embedding Cu single atoms on La-based nanoparticles (*p*-CNCu$^s$La$^n$-m). DFT analysis emphasizes the critical role of La-based clusters as proton donors in e-$NO_3$RR, while in situ characterization reveals an O-end adsorption reduction mechanism. The catalyst achieves a remarkable Faraday efficiency ($FE_{NH3}$) of 97.7%, producing 10.6 mol $g_{metal}^{-1}$ $h^{-1}$ of $NH_3$, surpassing most prior studies. In a flow cell, it demonstrated exceptional stability, with only a 9% decrease in current density after 111 hours and a $NH_3$ production rate of 1.57 $mg_{NH3}/h/cm^{-2}$. The proton donor mechanism's effectiveness highlights its potential for advancing electrocatalyst design. Beyond $NH_3$ production, the O-end mechanism opens avenues for exploring molecular-oriented coupling reactions in e-$NO_3$RR, paving the way for innovative electrochemical synthesis applications.**

## 1. Introduction

Ammonia ($NH_3$) is widely utilized in diverse industries, including chemical products, pharmaceuticals, fertilizers, and fuels, playing a fundamental role in contemporary society.[1–3] Currently, the dominant method for $NH_3$ production is the energy-intensive Haber-Bosch process.[4,5] This process requires high temperatures (≈500 °C) and pressures exceeding 100 atmospheres, resulting in substantial energy consumption and significant carbon dioxide emissions.[6–10] Consequently, there is an urgent need to develop environmentally friendly and sustainable methods for $NH_3$ synthesis. The electrochemical nitrate reduction reaction (e-$NO_3$RR) offers a promising alternative to NRR for synthesizing $NH_3$.[11–13] Unlike NRR, e-$NO_3$RR does not require overcoming the high-energy dissociation of the N≡N triple bond (941 kJ $mol^{-1}$). Instead, it involves breaking the N═O bond in nitrate ($NO_3^-$), which requires only 204 kJ $mol^{-1}$.[14–16] This lower energy requirement, combined with the high solubility of nitrates in solution, can significantly accelerate $NH_3$ synthesis. Moreover, nitrates are prevalent in industrial wastewater and contaminated groundwater, making e-$NO_3$RR a dual-purpose process that can aid in wastewater denitrification and enhance the nitrogen cycle in ecosystems.[17,18] Notably, the complexity of actual wastewater components, including organic matter and heavy metal ions, has the potential to compete with the e-$NO_3$RR, thereby influencing the reaction's progression.

The e-$NO_3$RR is a complex process involving eight electron transfers and various intermediates. While diverse catalysts have been explored for this reaction, there remains a scarcity of detailed studies on the structural changes in molecular adsorption between the intricate O and N intermediates and the catalyst during e-$NO_3$RR.[19–21] This challenge arises from the intricate forces at play between the NO intermediates and catalyst atoms, such as N-end, O-side, N-side, and O-end (as shown in **Figure 1**), making the precise control of e-$NO_3$RR pathways arduous.[4,22–24] As research on e-$NO_3$RR progresses, the coupling reactions (C-X, where X = N, P, S) of e-$NO_3$RR intermediates like hydroxylamine and primary amine with carbon sources to yield high-value chemicals have emerged as a significant research focus.[25–27] Notably,

Y. Zuo, M. Sun, L. Sun, B. Huang, X. Wang
Department of Chemistry
City University of Hong Kong
Hong Kong 999077, P. R. China
E-mail: bolhuang@cityu.edu.hk; wang.xin@cityu.edu.hk
M. Sun, B. Huang
Department of Applied Biology and Chemical Technology
The Hong Kong Polytechnic University
Hung Hom, Kowloon, Hong Kong 999077, P. R. China
T. Li
Institute of Surface Micro and Nano Materials
Xuchang University
Xuchang, Henan 461002, P. R. China
S. Han, Y. Chai
Department of Applied Physics
The Hong Kong Polytechnic University
Hong Kong 999077, P. R. China
The ORCID identification number(s) for the author(s) of this article can be found under https://doi.org/10.1002/adma.202415632



**DOI: 10.1002/adma.202415632**

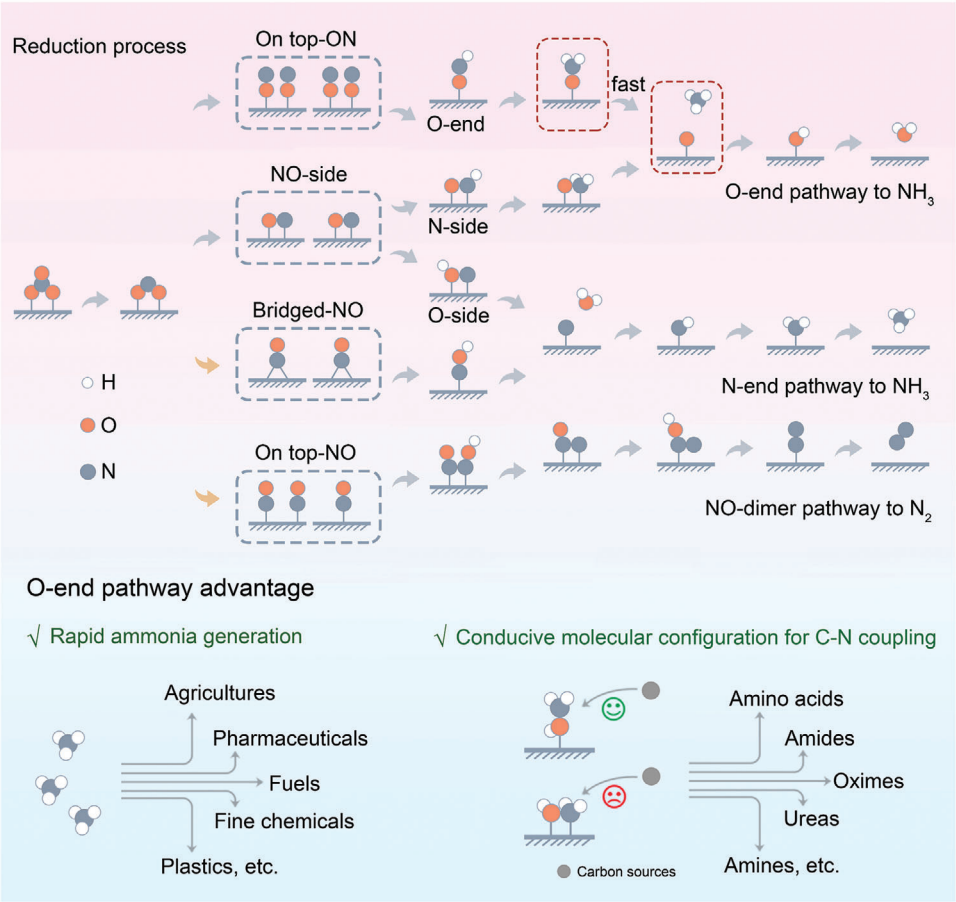


**Figure 1.** Illustration of the e-$NO_3^-$RR to $NH_3$, showcasing pathways such as N-end, O-side, N-side, and O-end, and the advantages of the molecular configuration within the O-end pathway.

the spatial molecular configuration of reaction intermediates is dictated by the interactions between NO intermediates and catalyst atoms.[28,29] In the O-end e-$NO_3$RR catalytic pathway, the exposed $^*$OH-$NH_2$ at the outer end facilitates spontaneous C-N coupling reactions with carbon sources (notably ketone groups), yielding high-value amino acids, oximes, amides, and other valuable products.[28,29] Therefore, the advancement of catalysts tailored for O-end e-$NO_3$RR pathways holds promise for enhancing $NH_3$ production and facilitating molecular-targeted C-X coupling electrochemical synthesis.

Cu-based catalysts exhibit high activity in the e-$NO_3$RR due to the alignment of their d orbital energy levels with the LUMO $\pi^*$ of $NO_3^-$, which facilitates electron transfer from the metal atoms to the adsorbed $NO_3^-$, thereby accelerating the reaction.[19,20] However, the limited capacity of Cu to supply electroactive hydrogen largely impedes the efficient hydrogenation and reduction of nitrogen intermediates (e.g., $^*NO_2$, NO, N), resulting in suboptimal Faraday efficiency of $NH_3$ formation ($FE_{NH3}$) with pure Cu catalysts.[21–23] Various strategies have been investigated to enhance the $FE_{NH3}$ of Cu catalysts, including the use of Cu-based alloy catalysts,[24,25] single-atom Cu configurations,[26,27] and Cu nanomaterials with diverse morphologies.[28,29] By introducing Cu single atoms ($Cu^s$) onto other nanoparticles, both high affinity to N-species intermediates and hydrogen supply can be ensured. La-based particles demonstrate moderate $H^*$ release capability under reducing potential conditions, offering rich active $H^*$ on the surface of La-based particles, which are able to spill over to the nearby active Cu sites, thus expediting hydrogenation of N-intermediates to form ammonia on Cu-based catalysts.[30–32] Such tandem catalytic synthesis of $NH_3$ requires an abundant supply of H atoms per nitrogen source, highlighting the importance of having proton donor around the nitrogen intermediates (e.g., $^*NO_2$, NO, N). Consequently, the integration of $Cu^s$ onto La-based nanoparticles is anticipated to enhance the e-$NO_3$RR activity of Cu sites and facilitate tandem catalysis for increased $NH_3$ production. In the design of binary alloy nanomaterials, the catalytic performance is intricately influenced by factors such as the alloy effect and strain, contributing to a complex structure-activity relationship within the catalytic system.[33,34] Additionally, the e-$NO_3$RR catalytic mechanism of Cu-based catalysts, particularly the binding modes with the nitrogen and oxygen ends in $NO_x$ intermediates, as well as the intricacies of the electron transfer process, remain enigmatic and warrant continuous exploration and elucidation.

Herein, this work synthesized porous N-doped carbon (*p*-CN) spheres loaded with $Cu^s$ incorporated La-based nanoparticles (*p*-CN$Cu^sLa^n$-m), using a combination of ultraviolet radiation reduction, confined synthesis, and microwave treatment, and

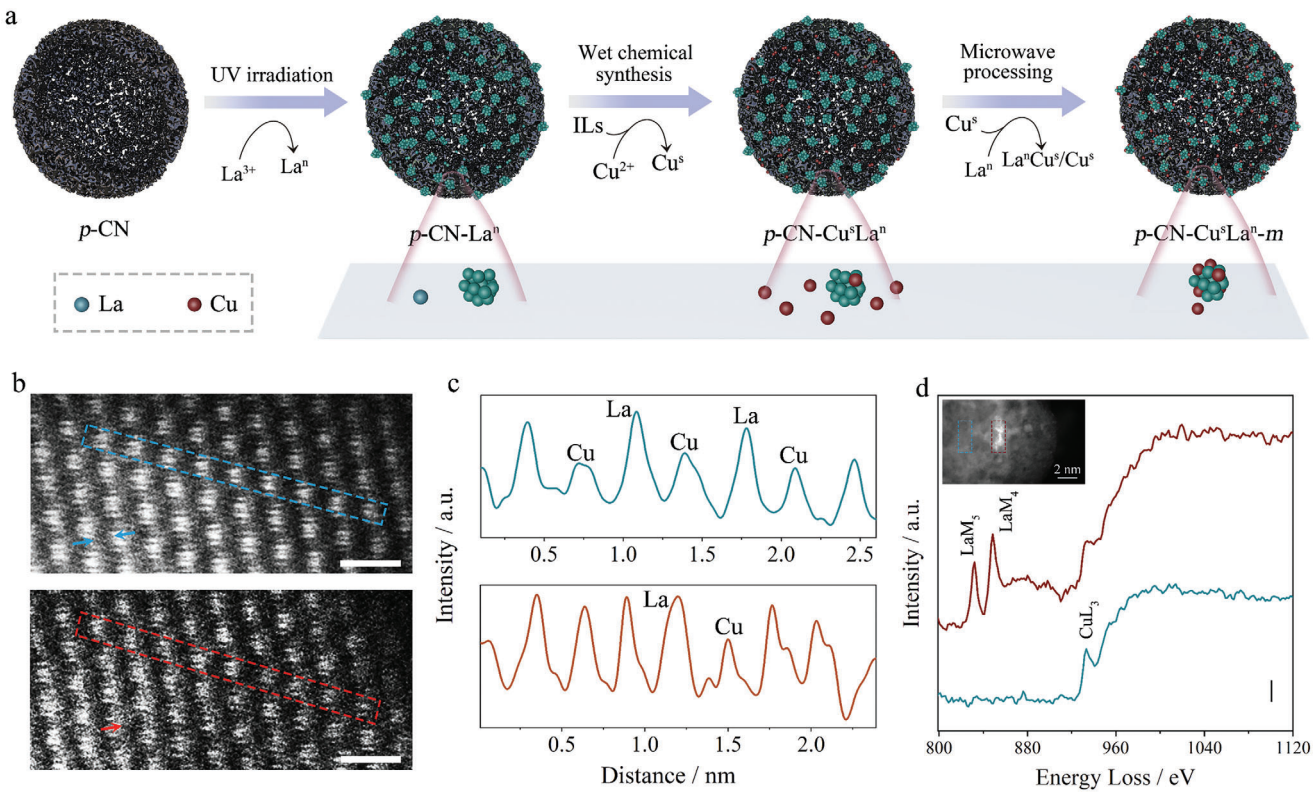


**Figure 2.** Materials synthesis and structural characterization analysis. a) Schematic illustrations of the preparation of *p*-CN-Cu$^s$La$^n$-m. b) Atomic resolution image of Cu$^s$La$^n$ nanoparticle. The scale bar represents 0.5 nm. c) The corresponding intensity profiles of lattice fringes along blue and red box in (b). d) EELS spectrum of *p*-CN-Cu$^s$La$^n$-m on the Cu$^s$La$^n$ and particle-free area.

evaluated their performance in electrochemical nitrate reduction (e-$NO_3$RR). By introducing Cu$^s$ into La nanoparticles, the bond between Cu and N atoms can be weakened and the Cu—O bonded form can be maintained, thereby selectively adsorbing NO intermediates. At the same time, La-based particles show moderate adsorption under reduction potential conditions.[30] The H$^*$ release ability can provide the catalyst with abundant active H$^*$, which can overflow to nearby active Cu sites, thus accelerating the hydrogenation of N intermediates on Cu sites.[31,32] The results of in situ Raman and in situ infrared show that the *p*-CNCu$^s$La$^n$-m is an O-end e-$NO_3$RR catalytic mechanism as shown in Figure 1, and the interaction between Cu atoms and La substrate significantly improves the catalytic activity under alkaline conditions. The e-$NO_3$RR efficiency achieves a significant $FE_{NH3}$ of 97.7%, producing 10.6 mol $g_{metal}^{-1}$ $h^{-1}$ of $NH_3$.

## 2. Results and Discussion

This study integrates ultraviolet radiation reduction, confined synthesis, and microwave treatment to capture Cu$^s$ on the surface of La-based nanostructure, as depicted in **Figure 2**a. La-based nanoparticles were first synthesized under ultraviolet reduction conditions using *p*-CN spheres as substrates. The *p*-CN features a variety of pore structures that serve as reaction cavities for the spatially constrained synthesis of single atoms.[35] As shown in Figure S1 (Supporting Information), heterogeneous nucleation initially presents a lower energy barrier compared to homogeneous nucleation.[36] Under ultraviolet irradiation, the CN substrate acts as an active site for the reaction, facilitating electron transfer to La ions to form La atoms, thereby enabling the loading and synthesis of La-based nanoparticles (*p*-CNLa$^n$). By leveraging the microporous of the *p*-CN as reaction cavities, double confinement synthesis strategy was applied to synthesize *p*-CNCu$^s$ with Cu$^s$ on *p*-CN and *p*-CNCu$^s$La$^n$ with Cu$^s$ in *p*-CNLa$^n$.[35] The notable specific surface area of *p*-CN facilitates the physical adsorption of Cu atoms with inadequate stability, resulting in the instability of *p*-CNCu$^s$La$^n$ and restricting the number of Cu atoms on La-based particles. To achieve a more stable dispersion of Cu atoms on the surface of La-based nanostructures, microwave treatment was utilized to induce the migration of Cu atoms to the surface of La-based nanoparticles, leading to the formation of *p*-CNCu$^s$La$^n$-m.

The X-ray diffraction (XRD) analysis (Figure S2, Supporting Information) of the synthesized samples reveals a characteristic CN broad peak within the 20–30° range. Comparatively, the XRD results of the *p*-CNCu$^s$ sample closely resemble those of *p*-CN, suggesting the absence of a crystalline structure in the obtained *p*-CNCu$^s$. In contrast, the XRD pattern of the *p*-CNLa$^n$ sample is compared with standard XRD data of La, LaN, and $La_2O_3$. The distinctive Bragg diffraction peak of *p*-CNLa$^n$ at 27.5° falls between the diffraction peaks associated with the (100) and (101) facets of metallic La. Similarly, the peak at 30.4° lies between La (102) and $La_2O_3$ (101), while the 31° peak is attributed to La (102), indicating that the nanoparticles in *p*-CNLa$^n$, *p*-CNCu$^s$La$^n$, and

*p*-CNCu$^s$La$^n$-m are partially oxidized La-based nanoparticles stabilized by the CN substrate.[37] TEM images in Figure S3 (Supporting Information) reveal that La-based nanoparticles were effectively deposited onto the surface of *p*-CN, with the size distribution from 30 to 80 nm. The energy dispersive spectrometry (EDS) line scan spectra (Figure S3e, Supporting Information) further illustrate the distribution of La within the *p*-CN matrix. HRTEM images (Figure S3b,c, Supporting Information) demonstrate that the La-based nanoparticles possess a dendritic aggregate structure. La atoms disperse and nucleate on the *p*-CN, forming atomic clusters. Subsequent deposition of La atoms leads to multi-site growth, culminating in the formation of dendritic La aggregates, as evidenced by the HRTEM results. TEM and scanning transmission electron microscopy (STEM) images in Figure S4 (Supporting Information) indicate that *p*-CNCu$^s$La$^n$ sample maintains a similar morphology to *p*-CNLa$^n$ with the dispersion of La-based nanoparticles on the surface of *p*-CN. The EDS line scan spectra (Figure S4e, Supporting Information) further illustrate the Cu is widely dispersed in *p*-CN. Interestingly, the HRTEM and STEM images in Figure S5 (Supporting Information) demonstrate the uniform dispersion of Cu$^s$La$^n$ nanoparticles with an average size of ≈3.8 nm after microwave treatment. Atomic-level STEM analysis (Figure 2b) reveals a lattice spacing of 0.287 nm for the loaded particle, attributed to the Cu$^s$La$^n$ (102) crystal plane which indicates the particles are still mainly La phase after microwave treatment. EDS mapping images (Figure S6, Supporting Information) indicate that there are numerous Cu atoms on La-based particles in the *p*-CNCu$^s$La$^n$-m. Besides, the relative intensity difference of the lattice fringes (Figure 2c) further verified the existence of Cu$^s$ on the surface of Cu$^s$La$^n$. Electron energy loss spectroscopy (EELS) measurements were conducted to probe the electronic structure of La and Cu in *p*-CNCu$^s$La$^n$-m. In Figure 2d, the typical La $M_{5,4}$ and Cu $L_{3,2}$ edge EELS spectra from the *p*-CNCu$^s$La$^n$-m sample are illustrated, showcasing a prominent spin-orbit splitting effect.[37,38] Within the loaded particle region of *p*-CNCu$^s$La$^n$-m, the EELS spectrum reveals characteristic La $M_4$ and $M_5$ edge spectral peaks around ≈832.1 eV and ≈848.6 eV, respectively. These peaks, which display a blue shift compared to $La_2O_3$ and proximity to La metal, indicate a shift in the 4f unoccupied state density of La atoms.[37,38] The Cu $L_3$ edge spectrum observed in the Cu$^s$La$^n$ particle, alongside the Cu $L_3$ edge spectrum peak at the CNCu$^s$ position (≈933.1 eV), suggests a lack of white edge in Cu within Cu$^s$La$^n$, implying a filled Cu3d band in this region.[39] This signifies the structural stability of the captured Cu single atoms in Cu$^s$La$^n$ particle. The presence of white lines indicates Cu binding to N at the CNCu$^s$ position, with the Cu 3d band showing partial occupancy.[39]

In order to further analyze the valence state of the elements in *p*-CN-Cu$^s$La$^n$-m sample and the coordination environment of Cu, X-ray photoelectron spectrometer (XPS) and X-ray absorption spectroscopy (XAS) measurements were used, and the results are shown in **Figure 3**. The charge effect was eliminated by correcting the binding energy (BE) of C1s to 284.8 eV. The XPS survey spectrum of *p*-CN-Cu$^s$La$^n$-m is shown in Figure S7 (Supporting Information), which confirmed the existence of C, N, Cu, and La in the *p*-CN-Cu$^s$La$^n$ and *p*-CN-Cu$^s$La$^n$-m. The Cu signal in *p*-CN-Cu$^s$La$^n$ sample appears notably weak, likely due to the low Cu metal content, which is evidenced by the ICP-MS, indicating a Cu content of only 1.02% in the *p*-CN-Cu$^s$La$^n$ (Table S1, Supporting Information). The high-resolution N 1s XPS spectra in Figure 3a indicate that *p*-CN-Cu$^s$La$^n$ and *p*-CN-Cu$^s$La$^n$-m contain four forms of N, namely pyrrolic-N (400.0 eV), pyridine-N (397.9 eV), graphite-N (401.4 eV), oxidized N (403.5 eV), and N-Cu/La (398.6 eV).[40,41] The percentage of N-metal increased from 7.05% in *p*-CN-Cu$^s$ (N-Cu), 10.74% in *p*-CN-La$^n$ (N-La), 11.52% in *p*-CN-Cu$^s$La$^n$ (N-Cu/La) to 18.50% in *p*-CN-Cu$^s$La$^n$-m (N-Cu/La) as shown in Figure 3c. Additionally, the BE position of the La 3d peak for *p*-CN-La$^n$ (848.43 eV) shift to 837.53 eV (*p*-CN-Cu$^s$La$^n$) and 836.83 eV (*p*-CN-Cu$^s$La$^n$-m), suggesting an increased proportion of La-Cu on the surface of La-based nanoparticles after microwave treatment.[42] XANES analysis can be employed to analyze the oxidation state of Cu atoms in *p*-CN-Cu$^s$, *p*-CN-Cu$^s$La$^n$, and *p*-CN-Cu$^s$La$^n$-m catalysts, by comparing the edge positions with Cu foil. Notably, the normalized XANES spectra of Cu K-edge (Figure 3d) under transmission mode showed higher absorption edges for *p*-CN-Cu$^s$La$^n$ and *p*-CN-Cu$^s$La$^n$-m in contrast to standard Cu foil, indicating an oxidized state for Cu elements in these samples. The fitted extended X-ray absorption fine structure (EXAFS) results of the Cu K-edge were adopted to further analyze the structural features of *p*-CN-Cu$^s$La$^n$-m (Figure 3e; Figure S8, Supporting Information) with the pertinent local atomic structural parameters are outlined in Table S2 (Supporting Information). EXAFS fitting analysis gives the coordination number and bond distance of Cu atoms in *p*-CN-Cu$^s$, *p*-CN-Cu$^s$La$^n$, and *p*-CN-Cu$^s$La$^n$-m samples relative to the neighboring scattering atoms, providing the first shell Cu-N coordination number and bond distance of 4.5 ± 0.2 and 1.5 ± 0.2 Å, suggesting the presence of isolated Cu atoms in these samples.[43] The wavelet transforms (WT) of Cu K-edge EXAFS results (Figure 3f–i) exhibit a contour intensity maximum at 4–7 Å$^{-1}$ in the k-space of *p*-CN-Cu$^s$, *p*-CN-Cu$^s$La$^n$ and *p*-CN-Cu$^s$La$^n$-m, indicating the first shell coordination of Cu-N. It is worth noting that at ≈7.0 Å$^{-1}$ in k-space, *p*-CN-Cu$^s$ has a weaker contour intensity value, indicating the presence of a small number of Cu clusters. For the *p*-CN-Cu$^s$La$^n$-m sample, there is a maximum and a second maximum value of the contour intensity at ≈6.0 Å$^{-1}$ and ≈11.0 Å$^{-1}$ in k-space, indicating the presence of Cu single atoms and a probable trace amount of Cu-La, in accordance with the TEM-EELS data.[43] This suggests that microwave treatment can facilitate the trapping of Cu sites on the CN-La$^n$ substrate.

The electrocatalytic e-$NO_3$RR performance of *p*-CN-La$^n$, *p*-CN-Cu$^s$, *p*-CN-Cu$^s$La$^n$, and *p*-CN-Cu$^s$La$^n$–m samples were systematically studied using a H-type cell with a three-electrode system. To enhance the accuracy of the potential supplied by the mercury oxide reference electrode during testing, 1 M KOH was employed as the electrolyte, aligning with the same concentration present in the internal KOH solution of the reference electrode to minimize the impact of the liquid junction potential. Prior to testing, the newly acquired reference electrode underwent calibration using a hydrogen reversible reaction, with the outcomes detailed in Figure S9 (Supporting Information). All data during the electrochemical test were performed without iR compensation. To initially discern the variances in the electrocatalytic performances of the prepared samples, the electrochemically active surface area (ECSA) was assessed through electric double layer capacitance ($C_{dl}$) measurements. As displayed in Figures S10 and S11 (Supporting Information), *p*-CN-Cu$^s$La$^n$–m shows

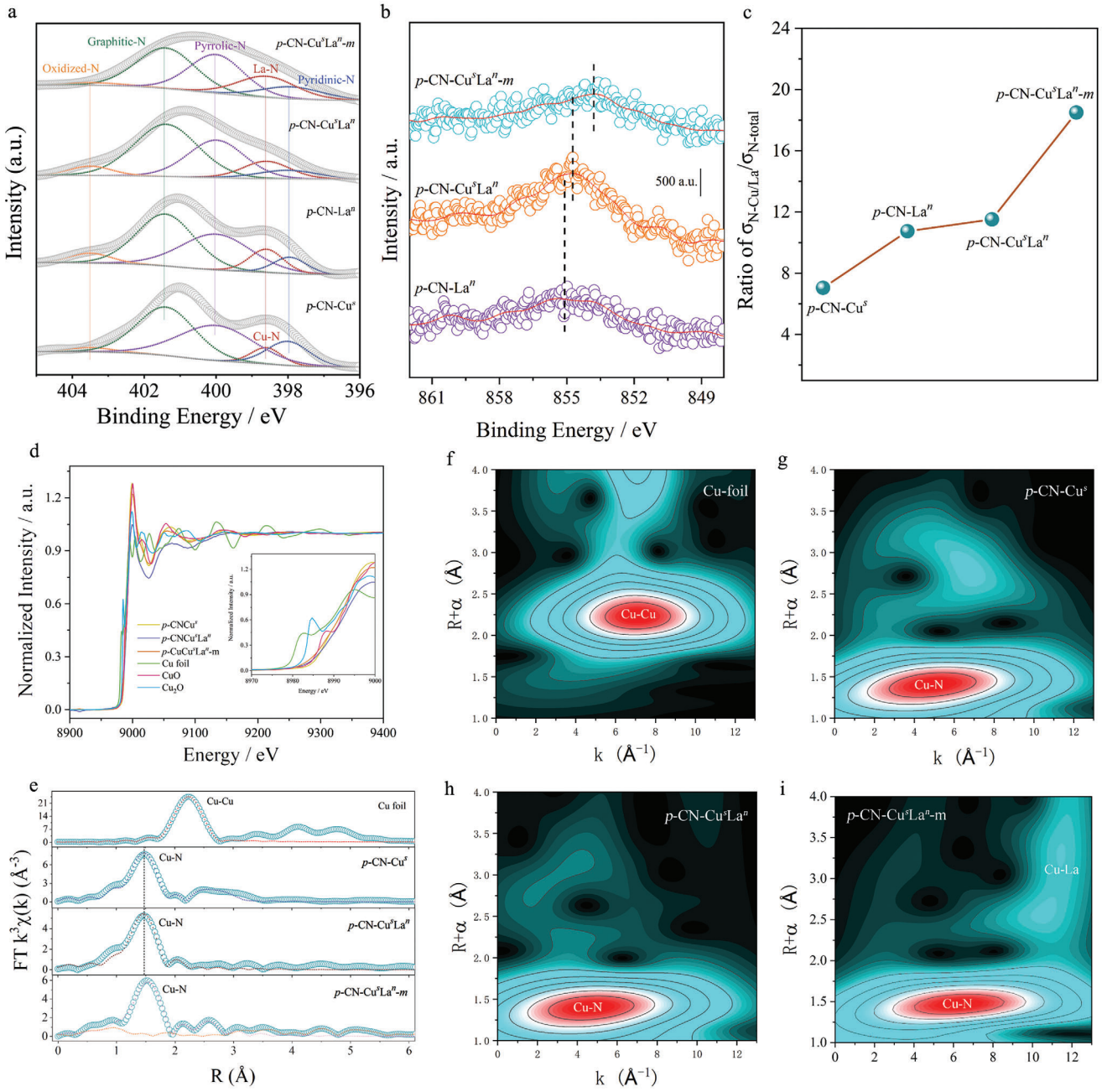


**Figure 3.** Analysis of the valence states and coordination environments of the elements in the prepared samples. a,b) The N 1s and La3d XPS results of the *p*-CN-Cu$^s$, *p*-CN-Cu$^s$La$^n$, and *p*-CN-Cu$^s$La$^n$-m. c) Ratio of $\sigma_{metal\text{-}N}/\sigma_{N\text{-}total}$ bonds. d) K-edge XANES spectra, e) Fourier transforms of k3-weighted EXAFS of the Cu foil, *p*-CN-Cu$^s$, *p*-CN-Cu$^s$La$^n$ and *p*-CN-Cu$^s$La$^n$-m. The red lines in (e) represents the EXAFS fitting curve of those samples. f–i) k3-weighted WT EXAFS spectra of the four corresponding samples.

the larger ECSA compared to *p*-CNCu$^s$ and *p*-CNCu$^s$La$^n$, revealing the more exposed active sites. Linear sweep voltammetry (LSV) profiles normalized to ECSA in **Figure** 4a and Figure S12 (Supporting Information) demonstrate that *p*-CN-Cu$^s$La$^n$–m exhibits the highest intrinsic e-$NO_3$RR activity among the catalysts, indicating that CNLa$^n$ captured Cu$^s$ can accelerate the e-$NO_3$RR reaction rate. The lowest Tafel slope and impedance of *p*-CN-Cu$^s$La$^n$–m sample (Figure 4b; Figure S13, Supporting Information) demonstrates its faster electron transfer frequency during e-$NO_3$RR. Three different colorimetric methods were used to determine the concentrations of $NH_3$, $NO_2^-$ and $N_2H_4$, respectively. The standard curves for $NH_3$, $NO_2^-$, $N_2H_4$ detection are shown in Figures S14–S16 (Supporting Information). Following chronoamperometric measurements, the production of $NH_3$ were analyzed and quantified using colorimetric method (Figure S17, Supporting Information). With the increase of potential, the $FE_{NH3}$ of *p*-CN-Cu$^s$ catalyst gradually increased (Figure 4c), but its $FE_{NH3}$ could only reach ≈70% under −0.5 V versus RHE,

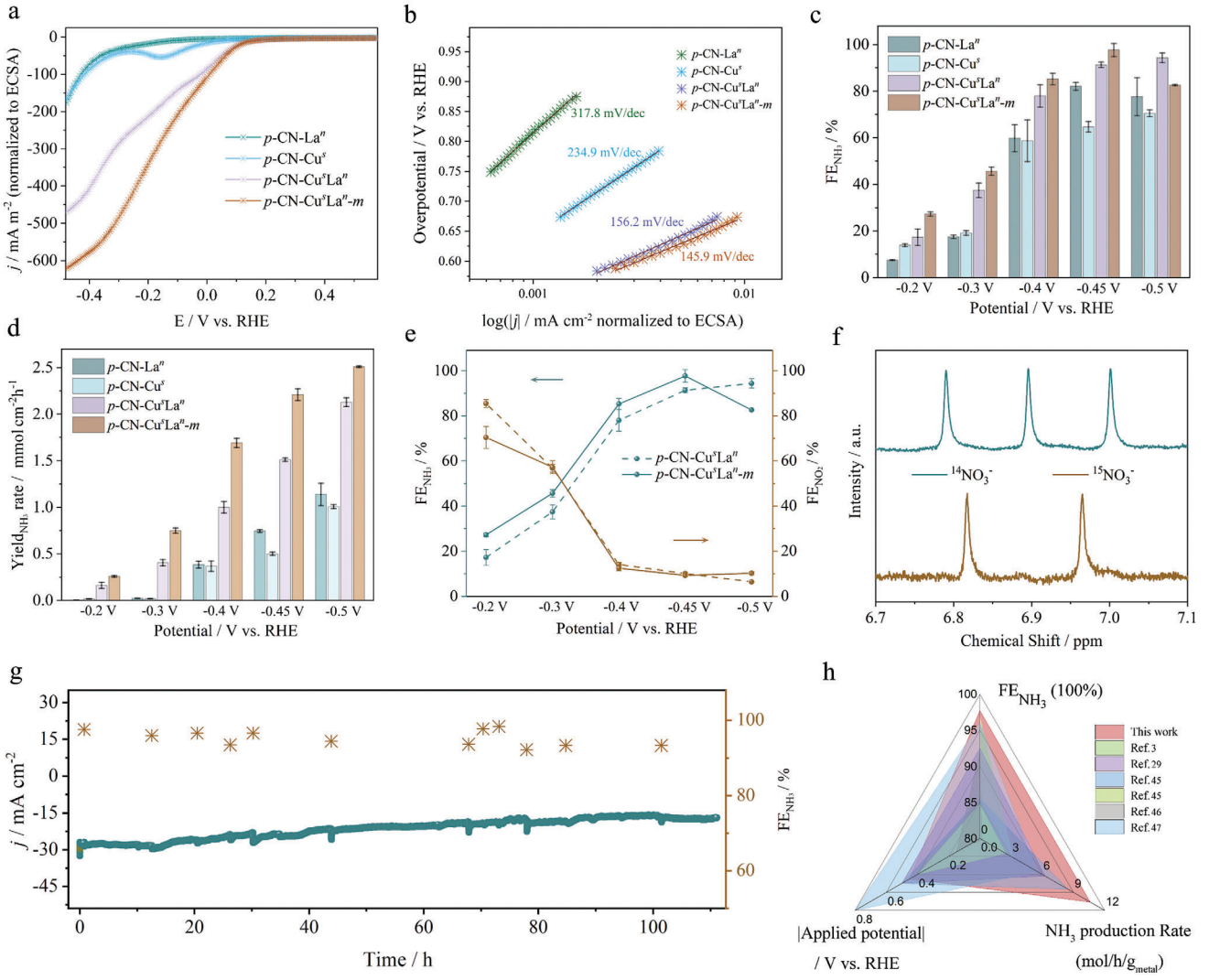


**Figure 4.** Electrocatalytic performance test in an H-type cell in 1 M KOH + 0.5 M $KNO_3$ electrolyte. a) LSV curves with a scan rate of 5 mV $s^{-1}$ normalized by geometric area of the electrode (1 $cm^2$). b) Tafel, c) $FE_{NH3}$, and d) $NH_3$ yield rates of *p*-CN-Cu$^s$, *p*-CN-Cu$^s$La$^n$, and *p*-CN-Cu$^s$La$^n$–m normalized by ECSA for the e-$NO_3$RR. e) $FE_{NH3}$ and $FE_{NO2}{}^-$ of *p*-CN-Cu$^s$La$^n$ and *p*-CN-Cu$^s$La$^n$–m under different voltage conditions. f) 1H NMR spectra of the products after e-$NO_3$RR, using $^{14}NO_3{}^-$and $^{15}NO_3{}^-$ as the nitrogen source. g) Long stability tests and h) A ternary spider chart illustrates the relationship between $FE_{NH3}$ (top), $NH_3$ production rate (right), and applied potential in the e-$NO_3$RR (left).

which was similar to other literature reports.[44] In the case of *p*-CNLa$^n$, within the range of 0 to −0.5 V versus RHE, a more negative potential leads to an increased formation of H$^*$ on the surface, eventually overflowing to the captured Cu$^s$ site for promoting the hydrogenation of $NO_2{}^-$ to form $NH_3$. *p*-CN-Cu$^s$La$^n$–m produced $NH_3$ with a high FE of 97.7 ± 2.8% at −0.45 V versus RHE, corresponding to the normalized yield by ECSA of 2.21 mmol $h^{-1}$ $cm^{-2}$ (Figure 4d), and normalized yield by mass of 289.4 ± 8.3 mmol $g_{cat}{}^{-1}$ $cm^{-2}$ $h^{-1}$ (Figure S18, Supporting Information). It is noteworthy that the *p*-CN-Cu$^s$La$^n$–m exhibit $NH_3$ yield reaching as high as 10.6 mol $g_{metal}{}^{-1}$ $h^{-1}$ when normalized to the metal loading (Figure S19, Supporting Information). $FE_{NO2}$- of *p*-CN-Cu$^s$La$^n$ and *p*-CN-Cu$^s$La$^n$–m samples continued to decrease with the increase of potential (Figure 4e), further verifying the change of $FE_{NH3}$. To verify the source of $NH_3$, we employed isotope-labeled $NO_3{}^-$ and combined with $^1$H nuclear magnetic resonance (NMR) analysis (Figure 4f), which confirmed that $NH_3$ products were generated from electrochemical e-$NO_3$RR rather than from any contamination. Figure 4g illustrates the long-term stability assessment of the *p*-CN-Cu$^s$La$^n$–m catalyst for e-$NO_3$RR. The current density of the *p*-CN-Cu$^s$La$^n$–m sample increased from the initial −29 to −18 mA $cm^{-2}$ after 110 h, meanwhile, the $FE_{NH3}$ derived from data at various time intervals remained largely consistent, underscoring the catalytic durability of *p*-CN-Cu$^s$La$^n$–m. The high-resolution HRTEM characterization results of the *p*-CN-Cu$^s$La$^n$–m post-stability test is depicted in Figure S20 (Supporting Information). These results indicate that the catalyst retains its original structure, affirming the structural stability of the low-coordination Cu atoms dispersed on the surface of the crystal. Subsequent atomic-resolution HRTEM results following stability assessments demonstrate the structural integrity and stability of Cu atoms on the La surface.

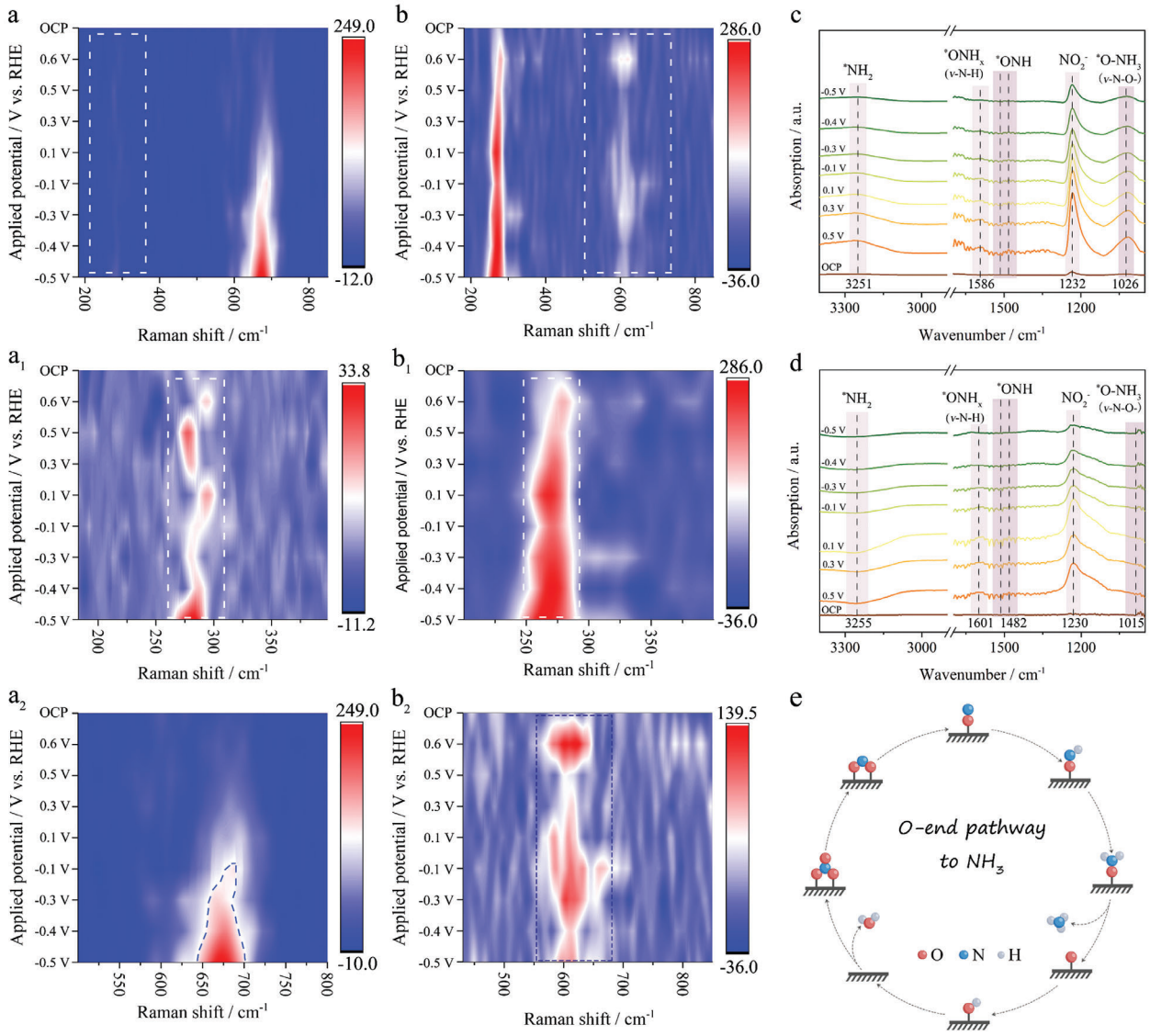


**Figure 5.** In situ electrochemical testing. a,b) Electrochemical in situ Raman spectra of e-$NO_3$RR of *p*-CN-Cu$^s$La$^n$ and *p*-CN-Cu$^s$La$^n$ –m as a function of potential and time. c,d) in situ ATR-SEIRAS spectra recorded over *p*-CN-Cu$^s$La$^n$ and *p*-CN-Cu$^s$La$^n$-m at different applied potentials (vs RHE). e) Schematic illustration showing the electrocatalytic $NO_3^-$-to-$NH_3$ reduction pathway on *p*-CN-Cu$^s$La$^n$-m.

Moreover, the notable stability observed in the flow cell emphasizes the significant practical promise of the prepared materials (Figure S21, Supporting Information). In comparison to the reported catalysts (Figure 4h; Table S3, Supporting Information), the synthesized samples have demonstrated competitive $FE_{NH3}$ and $NH_3$ yield (10.6 mol $g_{metal}^{-1}$ $h^{-1}$).[3,29,45–47]

To identify the reaction intermediates and elucidate the reaction mechanism of e-$NO_3$RR on *p*-CN-Cu$^s$La$^n$ and *p*-CN-Cu$^s$La$^n$–m, in situ Raman and attenuated total reflection surface-enhanced infrared spectroscopy (ATR-SEIRAS) measurements were performed. Raman spectra of e-$NO_3$RR on *p*-CN-Cu$^s$La$^n$ and *p*-CN-Cu$^s$La$^n$–m at potentials from 0.6 to −0.5 V versus RHE are shown in **Figure** 5a,b and Figure S22 (Supporting Information). The weak broad peak at 280.3 $cm^{-1}$ of *p*-CN-Cu$^s$La$^n$ is classified as the vibration peak of La-O or La-$ON_x$, while the strong peak at 693.4 $cm^{-1}$ is Cu-O or Cu-$ON_x$.[48–50] Unlike *p*-CN-Cu$^s$La$^n$, *p*-CN-Cu$^s$La$^n$–m has a strong La-O peak at 272.5 $cm^{-1}$, and a weak Cu-O peak at 642.5 $cm^{-1}$.[48–50] The vibration intensity of the La—O bond in *p*-CN-Cu$^s$La$^n$-m is significantly stronger than that of *p*-CN-Cu$^s$La$^n$, which indicates that the particle size of La particles becomes smaller and more atoms are exposed at the interface as a result of microwave treatment. As the potential gradually shifts toward more negative value, the bond vibration of Cu—O on the Cu site in *p*-CN-Cu$^s$La$^n$ becomes stronger. Under the reduction potential conditions, the oxide or hydroxide of Cu is very easy to be reduced to $Cu^0$ valence state. The large number of Cu-O bonds indicates the mechanism path of e-$NO_3$RR at the Cu site is the O-end path.[4,15] The ATR-SEIRAS spectrum of e-$NO_3$RR at a potential of 0.5 to −0.5 V versus RHE shows that different nitrogen-containing intermediates appear in the spectrum. The peaks at

1026 and 1232 $cm^{-1}$ in Figure 5c,d can be attributed to the stretching vibration modes of $^*N\text{-}OH_x$ and $^*N\text{-}O$, respectively.[3,27,51] Furthermore, the peaks at 1500 and 1586 $cm^{-1}$ can be assigned to the stretching vibration mode of $^*N = O$ and the bending vibration mode of $^*NH_2\text{-}OH$, respectively.[3,27,50] Additionally, the peak at 3251 $cm^{-1}$ can be attributed to the stretching vibration mode of secondary ammonia $^*N\text{-}H$.[3,27,51] Based on in situ Raman and ATR-SEIRAS results, the proposed e-$NO_3$RR pathway on *p*-CN-$Cu^sLa^n$–m was displayed in Figure 5e. After $NO_3^-$ was adsorbed on *p*-CN-$Cu^sLa^n$–m, it first undergoes a series of deoxygenation reactions from $NO_3^*$ to $NO_2^*$ and then to $NO^*$ on the catalytic active center. After the NO intermediate is finally formed at the interface, the molecular configuration changes to form an O-end adsorption, and the N atom is connected to O but not directly bonded to the active center. In contrast to the previous O-end mechanism, once the intermediate product $^*ONH_2$ is formed, the H intermediate generated from the La site will react with O and $NH_2$ intermediates, which readily yield the final product $NH_3$.

To further understand the origins of superior e-$NO_3$RR performances of *p*-CN-$Cu^sLa^n$–m, we have carried out theoretical investigations based on DFT calculations to understand the origins of superior e-$NO_3$RR performances of *p*-CN-$Cu^sLa^n$–m by comparing with *p*-CN-$La^n$, and (c) *p*-CN-$Cu^s$ (Figure S23, Supporting Information). To reveal the surface electroactivity, the electronic distributions regarding the bonding and anti-bonding orbitals near the Fermi level ($E_F$) are demonstrated. For *p*-CN-$Cu^sLa^n$–m, we notice that the surface La cluster with atomic dispersion of Cu contributes to the bonding orbitals (**Figure 6a**). The carbon support with $Cu^s$ also shows contributions to the bonding orbitals, supporting the high electron transfer and exchange capability of the surface. Without the $Cu^s$, the anti-bonding orbitals become more evident on the *p*-CN-$La^n$ surface even for the carbon support, leading to the reduced electroactivity for e-$NO_3$RR (Figure 6b). The electroactivity has been further reduced in *p*-CN-$Cu^s$, where the anti-bonding orbitals become dominant on the surface (Figure 6c). To demonstrate the different electronic structures, we have compared the projected partial density of states (PDOS) of *p*-CN-$Cu^sLa^n$–m, *p*-CN-$La^n$, and *p*-CN-$Cu^s$. For *p*-CN-$Cu^sLa^n$–m, La-5d orbitals are located near the $E_F$ while the Cu-3d orbitals display a sharp peak near $E_V$-2.95 eV ($E_V$ denotes 0 eV) (Figure 6d). The La sites facilitate the electron transfer efficiency and the Cu sites play as the main active sites to bind with N species during e-$NO_3$RR, which collectively benefit the e-$NO_3$RR. The 2p orbitals of the carbon support cover a broad range to promote site-to-site electron transfer. For *p*-CN-$La^n$, although the La-5d orbitals are still located near $E_F$, there is a lack of electron-rich sites with strong reduction capability to facilitate the reduction of $NO_3^-$ (Figure 6e). In *p*-CN-$La^n$, the 2p orbitals of the carbon support are more electron-rich, but it cannot supply sufficient reduction trends for $NO_3^-$, resulting in strongly reduced electroactivity. For *p*-CN-$Cu^s$, the Cu-3d orbitals are upshifted toward the $E_F$ when compared with *p*-CN-$Cu^sLa^n$–m, representing a slightly higher valence state as characterized by the experiments (Figure 6f). The good overlapping between Cu-3d and 2p orbitals of carbon supports are noted. However, the low electron density near the $E_F$ cannot guarantee an efficient electron transfer, which also largely decreases the e-$NO_3$RR performance. The PDOS results have indicated the synergistic effect of $Cu^s$ and La clusters for e-$NO_3$RR. To obtain an in-depth understanding of the electronic structures in *p*-CN-$Cu^sLa^n$–m, we have shown the site-dependent PDOS with different environments (Figure 6g; Figure S24, Supporting Information). From the interface regions to the top surface, the electroactivity of Cu sites is highly correlated to the coordination number with neighboring La atoms. With the increasing CN with La, the Cu-3d orbitals downshift and become more electron-rich while the low-coordinated atoms such as $Cu^s$ on carbon support or edge of La clusters display the closest positions to the $E_F$. This confirms that lower coordinated $Cu^s$ is significant to achieve the high electroactivity of *p*-CN-$Cu^sLa^n$–m. Meanwhile, the La sites strongly vary at different positions, which further affects the electroactivity of La-5d orbitals (Figure 6h). The interfacial La sites show strong interactions with *p*-CN, displaying a broad distribution of La-5d orbitals. Owing to the similar high coordination number, both La-5d orbitals are similar for interface and center La sites. The surface La site is selected from the middle layer to compare with the edge sites of the surface layer. Notably, with the reducing coordination number, the electron density of La-5d orbitals near the $E_F$ is significantly improved, which strongly facilitates the electron transfer efficiency from the c to the intermediates, supporting the improved reaction kinetics as well. These results confirm that the electroactivity of both Cu and La sites are correlated with the coordination environment, whereas the abundant edge sites with low coordination numbers in $Cu^sLa^n$ nanoparticles supply highly electroactive sites to promote the e-$NO_3$RR. The PDOS evolutions also confirm the distinct electroactivity during the conversion of key intermediates (Figure 6i,j). For *p*-CN-$Cu^sLa^n$–m, the downshifting of 2p orbitals of N-species is noted, which indicates the faster conversion from $NO_3^*$ to $NO^*$. In comparison, the continuous downshifting trend is interrupted in CN-La from $NO_2^*$ to $NO^*$, which potentially induces energy barriers for this conversion during the e-$NO_3$RR. The superior e-$NO_3$RR performance of *p*-CN-$Cu^sLa^n$–m is attributed to the co-existence of $Cu^s$ and La clusters to supply sufficient active sites and fast site-to-site electron transfer. Then, we further carry out explorations from the energetic perspective to study the e-$NO_3$RR process. The fast e-$NO_3$RR not only requires the strong adsorptions of $NO_3^-$ but also the $H_2O$ to initiate the dissociation for fast proton supply during the reduction. Notably, the *p*-CN-$Cu^sLa^n$–m exhibits the largely enhanced adsorptions of nitrate, which is ascribed to the introduction of $Cu^s$ as the active sites (Figure 6k). For the $H_2O$ adsorption, we notice that the *p*-CN-$La^n$ shows a slightly stronger trend, which confirms that the La clusters play a critical role in the proton supply during the e-$NO_3$RR. The adsorption configurations of key intermediates reveal that the Cu-La sites play as the main active sites for the e-$NO_3$RR, where Cu facilitates the adsorption of intermediates while La sites promote the generation of active hydrogen from water dissociation (Figures S25 and S26, Supporting Information). Accordingly, we have compared the reaction energy trends of e-$NO_3$RR on both *p*-CN-$Cu^sLa^n$–m and *p*-CN-$La^n$ (Figure 6l; Figure S26, Supporting Information). It is noted that *p*-CN-$Cu^sLa^n$–m displays a highly energetic favored trend for the reduction of $NO_3^-$ to $NO^*$ while there is a large energy barrier of 0.56 eV for $NO_2^*$ conversion to $NO^*$ on *p*-CN-$La^n$, which agrees well with the PDOS results. The hydrogenation from $NH_2O^*$ to $NH_2OH^*$ is the rate-determining step for *p*-CN-$Cu^sLa^n$–m with an energy barrier of 0.29 eV, which is much lower

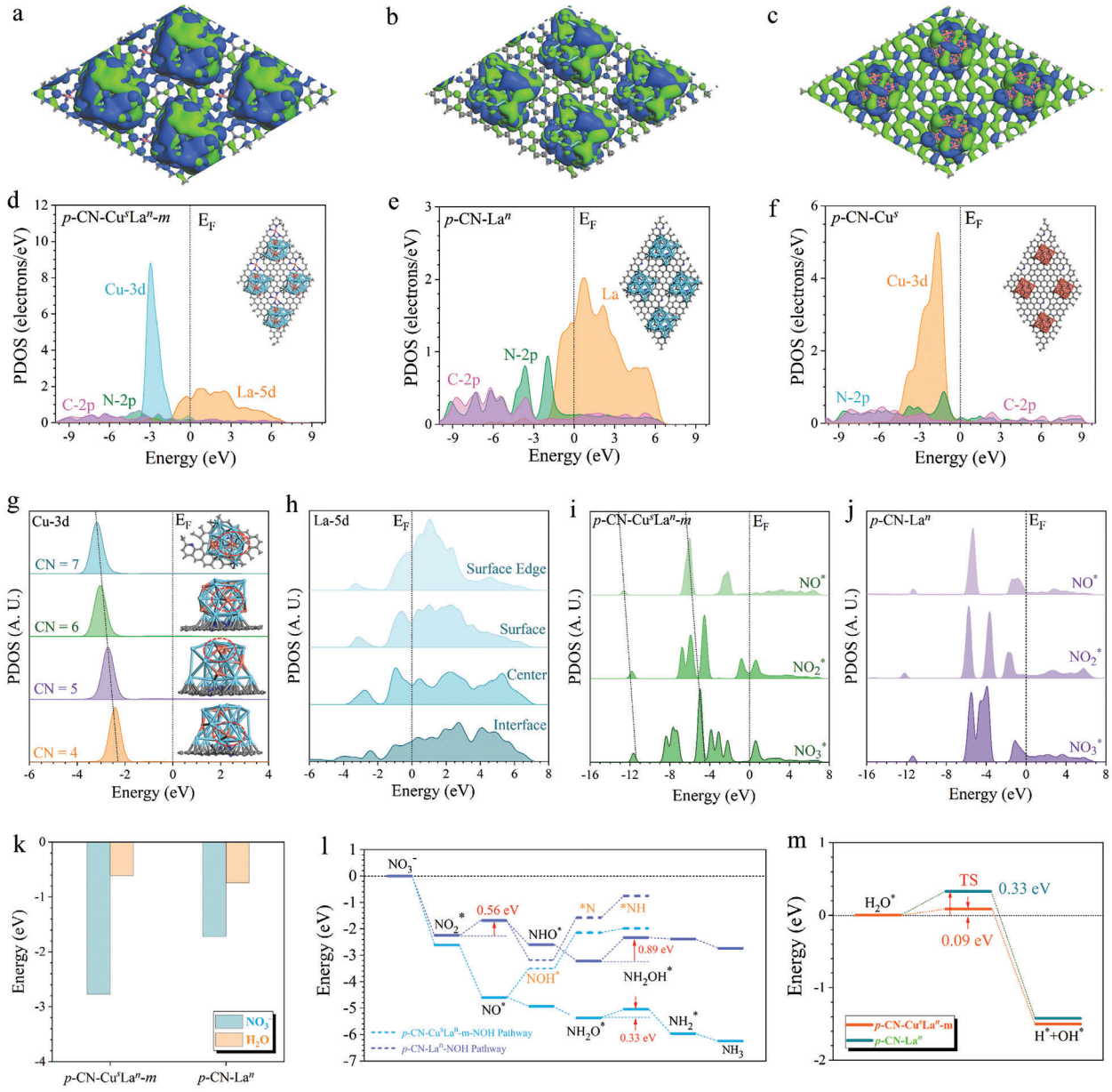


**Figure 6.** Density functional theory analysis of catalytic mechanism. The electronic distributions of bonding and anti-bonding orbitals near Fermi level on a) *p*-CN-Cu$^s$La$^n$–m, b) *p*-CN-La$^n$, c) *p*-CN-Cu$^s$. Blue isosurface = bonding orbitals, and green isosurface = anti-bonding orbitals. PDOS of d) *p*-CN-Cu$^s$La$^n$–m, e) *p*-CN-La$^n$, f) *p*-CN-Cu$^s$. Insets are structures after geometry optimizations. Orange balls = Cu, Light blue balls = La, grey balls = C, blue balls = N, and white balls = H. Site-dependent PDOS of g) Cu-3d and h) La-5d in *p*-CN-Cu$^s$La$^n$–m. The PDOS of key intermediates during e-$NO_3$RR in (i) *p*-CN-Cu$^s$La$^n$–m and j) *p*-CN-La$^n$. k) The adsorption energies comparisons of $NO_3^-$ and $H_2O$. l) The reaction energy trends of $NO_3^-$RR on *p*-CN-Cu$^s$La$^n$–m and *p*-CN-La$^n$ of different reaction pathways. m) The dissociation barriers of water in *p*-CN-Cu$^s$La$^n$–m and *p*-CN-La$^n$.

than that in *p*-CN-La$^n$, supporting the improved e-$NO_3$RR performance. The competition of different reaction pathways occurs at the hydrogenation step of NO*, where *p*-CN-Cu$^s$La$^n$–m and *p*-CN-La$^n$ prefer the formation of NHO* and NOH*, respectively. It is apparent that the NOH* pathway displays continuous barriers on *p*-CN-Cu$^s$La$^n$–m and *p*-CN-La$^n$ until the formation of NH*, indicating the high selectivity of the NHO* pathway. For *p*-CN-La$^n$, although the formation of NOH* is slightly more preferred, the large barrier for N* generation also limits the selectivity of the NOH* pathway. For the transition states (TS), we have noted that the overall activation barriers of *p*-CN-La$^n$ are much larger than that of *p*-CN-Cu$^s$La$^n$–m, indicating the faster electron transfer dynamic in *p*-CN-Cu$^s$La$^n$–m. (Figure S27, Supporting Information). Moreover, the activation energies of TS become the largest at the conversion from $NH_2O$* to $NH_2OH$, which is considered to be the rate-determining step (RDS) for both *p*-CN-Cu$^s$La$^n$–m and *p*-CN-La$^n$. More importantly, the overall e-$NO_3$RR is much more exothermic in *p*-CN-Cu$^s$La$^n$–m than *p*-CN-La$^n$, leading to the

increased selectivity and yield of $NH_3$. Additionally, the proton supply by water dissociation on *p*-CN-Cu$^s$La$^n$–m is also easier with a low barrier (0.09 eV) of the TS (Figure 6m). Notably, water decomposition on the La sites to generate protons, leading to the formation of O$^*$ intermediates on the catalyst surface. This observation aligns with in situ Raman data, which reveals a distinct metal-O vibration peak at elevated potential levels. In contrast, the increased barrier of TS (0.33 eV) for *p*-CN-La$^n$ affects the proton supply and reduces the e-$NO_3$RR activity. Based on the activation energy for the TS, the *p*-CN-Cu$^s$La$^n$–m displays much higher reaction rate constants *k* for both e-$NO_3$RR and water dissociation, which represents the much faster reaction kinetics and supports the Tafel plot results by experiments (Table S4, Supporting Information).

## 3. Conclusion

In summary, we have proposed a proton donor strategy to enhance the reactivity of Cu metal sites for e-$NO_3$RR. The *p*-CNCu$^s$La$^n$–m exhibited exceptional catalytic performance (achieving a FE of 97.7% and a yield of 10.6 mol $g_{metal}^{-1}$ $h^{-1}$. in situ electrochemical ATR-SEIRAS and in situ electrochemical Raman spectroscopic tests indicated that the e-$NO_3$RR mechanism on this catalyst followed an O-end route process. DFT calculations revealed that low-coordinated Cu displayed high electroactivity toward e-$NO_3$RR, while La sites provided a conducive electron transfer environment and efficient hydrogen supply capacity, thereby enhancing the efficiency of e-$NO_3$RR. The synergistic effect of low-coordinated Cu and La amplified adsorption of crucial intermediates, lowered the energy barrier and accelerated the e-$NO_3$RR reaction. Long-term stability assessments in H cells and flow cells confirmed the robust structural stability of the developed materials. This study not only presents a reaction pathway to enhance the e-$NO_3$RR activity of Cu-based materials but also offers insights for designing for designing proton donor cooperated functional catalysts for synergistic catalytic system. Specifically, this offers a foundational synthesis approach and design concepts for functional lanthanide metal nanomaterials, facilitating the integration of catalysts containing lanthanide elements in NRR, e-$NO_3$RR, and C-N coupled electrosynthesis systems reliant on these reactions.

## 4. Experimental Section

*Chemicals*: All chemical reagents were utilized as received without additional purification. Lanthanum nitrate hexahydrate ($La(NO_3)_3{\bullet}6H_2O$, >99%), sodium salicylate (99%), copper(II) nitrate trihydrate, potassium sodium tartrate tetrahydrate (99%), sodium hypochlorite solution (NaClO), $^{15}N$ labelled $NH_4Cl$ (98 atom % $^{15}N$), and concentrated phosphoric acid ($H_3PO_4$, >85wt%) were obtained from Sigma-Aldrich. Ethylene glycol (≥99.5%), potassium chloride (KCl, 99%), potassium hydroxide (KOH, AR, >85%), 1-Butyl-3-methylimidazolium hexafluorophosphate, sodium borohydride, potassium nitrate ($KNO_3$, 99%) were all purchased from Sino-pharm Chemical Reagent Co., Ltd. China. Sulfanilamide (99%), sodium nitroprusside (>99%), N-(1-naphthyl)ethylenediamine dihydrochloride (99%), and p-(dimethylamino)benzaldehyde (99%) were purchased from Adamas-Beta. Hydrazine (85%) was bought from Thermo Fisher Scientific Inc. The water used in all experiments was de-ionized.

*Material Characterizations*: Scanning electron microscopy (SEM) images were taken on an electron microscope, scanning (QUATTRO S), Thermo Scientifi at 15 kV. Transmission electron microscopy (TEM), atomic resolution TEM, and EDX elemental mapping were collected on a JEM-ARM-200F microscope operated at 200 kV and an FEI Titan HRTEM microscope operated at 300 kV. Powder X-ray diffraction (XRD) patterns were recorded through an X-ray diffractometer (Rigaku SmartLab) using Cu K$\alpha$ ($\lambda$ = 1.5418 Å) radiation. Inductively coupled plasma mass spectrometry (ICP-MS) was tested by an Agilent-7900 system. X-ray photoelectron spectra (XPS) were tested on a Thermo Scientific Escalab 250Xi X-ray photoelectron spectrometer, using non-monochromatized Al-K$\alpha$ X-ray (1486.6 eV) as the excitation source. The isotope labeling experiments were collected through $^1$H-NMR measurement (Bruker 600 MHz system). The Raman spectra were tested by Japan HORIBA LabRAM HR Evolution Raman spectrometer. Fourier transform infrared spectroscopy (FTIR) was measured by a Bruker VERTEX 80v with an MCT detector. UV–vis spectrum testing is performed using the SHIMADZU UV-1900i instrument. The X-ray absorption spectra at the Cu K-edge were recorded at the XAS station (BL 14W1) of the Shanghai Synchrotron Radiation Facility (SSRF). The data were processed by the ATHENA module and fitted by the ARTEMIS module in the IFEFFIT software package with a Hanning window (dk = 1.0 Å$^{-1}$).[52]

*Preparation of p-CNLa$^n$*: *p*-CN was synthesized based on the previously reported method.[35] 30 mg of *p*-CN powder and ≈7 mg $La(NO_3)_3{\bullet}6H_2O$ was dispersed in a solution of 8 mL ethylene glycol and 8 mL deionized water, then transferred to a watch glass with a diameter of ≈12 cm. The mixture was exposed to UV light for 5 min under shaking and repeated three times. The resulting product was thoroughly washed through multiple centrifugation steps using ethanol and deionized water, yielding the final product identified as *p*-CNLa$^n$.

*Preparation of p-CNCu$^s$La$^n$ and p-CNCu$^s$*: *p*-CNLa$^n$ material (20 mg) was firstly dispersed in the 1-butyl-3-methylimidazole hexafluorophosphate. Then ≈4 mg of $Cu(NO_3)_2{\bullet}3H_2O$ and a suitable amount of $H_2O$ were added and ultrasonicated for 30 min. Then the *p*-CNLa$^n$&Cu complex was collected by centrifugation and the precipitate was further dispersed in the $H_2O$, and then sodium borohydride ($NaBH_4$) was added to obtain *p*-CNCu$^s$La$^n$. For the synthesis of *p*-CNCu$^s$ sample, the *p*-CN powder was employed to place *p*-CNLa$^n$ and the remaining procedures are analogous.

*Preparation of p-CNCu$^s$La$^n$-m*: The *p*-CNCu$^s$La$^n$ powder was placed in a glass container, mixed with an adequate quantity of deionized water to create a paste. Subsequently, the mixture was transferred to a microwave oven and heated for 90 s.

*Ammonia ($NH_3$) Detection*: $NH_3$ detection was conducted using the indophenol blue method. Three solutions were prepared in advance.

Solution A was created by combining 5 g of sodium salicylate and 5 g of potassium sodium tartrate tetrahydrate with 100 mL of 1 M KOH solution.

Solution B was 0.05 M NaClO solution.

Solution C was 0.01 g mL$^{-1}$ sodium nitroprusside solution.

For the detection of $NH_3$, 2 mL of the reaction solution was diluted in 1 M KOH solution based on charge of the chronoamperometry test. Subsequently, the solution was mixed with 2 mL of solution A. Following this, 1 mL of solution B and 0.2 mL of solution C were sequentially added to the aforementioned mixture. After allowing it to stand for 2 h, the absorption spectrum of the solution was measured using a UV–vis spectrophotometer (SHIMADZU UV-1900i). The quantity of generated $NH_3$ was determined based on the absorbance value at a wavelength of 655 nm.

*Nitrite ($NO_2^-$) Detection*: Nitrite ($NO_2^-$) detection was conducted using the Griess method. The color reagent was prepared by combining 1 g of sulfanilamide, 0.1 g of N-(1-naphthyl)ethylenediamine dihydrochloride, and 2.94 mL of $H_3PO_4$ in 50 mL of deionized (DI) water.

Subsequently, 1 mL of the diluted reaction solution and 1 mL of the color reagent were added to 2 mL of DI water and left to stand for 20 min. The resulting solution was analyzed using a UV–vis spectrophotometer to quantify the generated $NO_2^-$ by measuring the absorbance value at a wavelength of 540 nm.

*Hydrazine ($N_2H_4$) Detection*: $N_2H_4$ detection was carried out using the Watt and Chrisp method. The color reagent was prepared by mixing 5.99 g of p-(dimethylamino)benzaldehyde, 30 mL of concentrated HCl,

and 300 mL of ethanol. Initially, 5 mL of the reaction solution was neutralized with an HCl solution and then combined with 5 mL of the prepared color reagent. The resulting solution was stirred for 20 min and subsequently analyzed using a UV–vis spectrophotometer to quantify the generated $N_2H_4$ based on the absorbance value at a wavelength of 460 nm.

The $FE_{NH3}$ was determined using the formula:

$$Q = Q_{NH3}/Q = n_{NH3} V c_{NH3} F/Q \quad (1)$$

where Q represents the applied overall coulomb quantity (C), $Q_{NH3}$ is the coulomb required to produce $NH_3$, n is the electron-transfer number (for 1 mol $NH_3$, it is 8), V is the volume of the catholyte of the cathode chamber (25 ml), $c_{NH3}$ is the concentration of $NH_3$ produced, and F is the Faraday constant (96485 C $mol^{-1}$).

*Electrochemical Measurements*: The electrochemical measurements for the e-$NO_3$RR were conducted using an Autolab PGSTAT302N electrochemical workstation. A mercury oxide (Hg/HgO) reference electrode and a platinum sheet served as the reference and counter electrodes, respectively.

To prepare the catalyst ink, 5 mg of the sample was dispersed in a mixture of 500 mL isopropanol and 500 mL $H_2O$ along with 100 µL of 5 wt.% Nafion. The mixture was sonicated for 30 min to achieve a homogeneous ink. The catalyst was then loaded onto a hydrophobic carbon paper with a geometric area of 1 $cm^{-2}$ using spray coating. Linear sweep voltammetry and chronoamperometry tests were performed in the H-cell with the electrolyte comprising 1 M KOH + 0.5 M $KNO_3$.

*In Situ ATR-FTIR Tests*: In situ ATR-FTIR tests were performed using a Bruker V80 instrument equipped with an electrochemical VeeMax III apparatus from PIKE. A liquid nitrogen-cooled mercury cadmium telluride (MCT) detector was utilized. A silicon prism coated with a thin Au layer was employed to reflect the signal. In situ signals were then recorded at various potentials.

*Calculation Setup*: To investigate the e-$NO_3$RR performances of CN-CuLa, the density functional theory (DFT) calculations were applied based on the CASTEP packages.[53] The generalized gradient approximation (GGA) and Perdew–Burke–Ernzerhof (PBE) functionals were selected to supply accurate descriptions of the exchange-correlation interactions.[54–56] For the geometry optimizations, the ultrasoft pseudopotentials were chosen and the cutoff energy was set to 440 eV based on the ultrafine quality. The k-point is applied with 0.05 1/Å separation with the Broyden-Fletcher-Goldfarb-Shannon (BFGS) algorithm for all the energy minimizations in this work.[57] During the geometry optimizations, we have considered stringent convergency criteria including the Hellmann-Feynman forces should not exceed 0.001 eV $Å^{-1}$ and the total energy difference should be converged to smaller than $5 \times 10^{-5}$ eV/atom. For the model building, the substrate *p*-CN was built on a single graphene in a 6×6×1 supercell with vacancies and N-doped carbon unit in the structure. For the $La^n$ anchored on the *p*-CN substrate, the cluster was cleaved from the (100) surface with a three-layer thickness including 23 La atoms. To construct the $Cu^sLa^n$ nanoparticle, 5 Cu atoms have been introduced to replace the La atoms on the surface, which are atomically dispersed in the nanoparticle. Meanwhile, the $Cu^s$ was also cleaved from (100) surface with four-layer thickness.

For the calculations of the reaction energy, the following equation is applied:

$$\Delta G = \Delta E + \Delta ZPE - T\Delta S \quad (2)$$

For Equation (2), $\Delta E$ is the reaction energy calculated from the DFT based on the final enthalpy of the reactants and products of each step. Meanwhile, the $\Delta ZPE$ and $\Delta S$ are the changes of the zero point energy and entropy, respectively at T = 298 K and 1 atm.

The activation energies ($E_a$) of transition states (TS) are further evaluated by the TS searching methods embedded in CASTEP through the complete LST/QST protocol. The maximum QST step is set to 5. To discuss the reaction kinetics, the study have further calculated the reaction rate constants based on the following equation.

$$k = \frac{k_b T}{h}\left(\frac{p^0}{RT}\right)^{n-1} \exp\left(\frac{-E_a}{RT}\right) \quad (3)$$

In this equation, $E_a$ represents the activation energy of the reaction step, $k_b$ is the Boltzmann constant, *h* is the plank constant, R is the gas constant, T is the reaction temperature, $p^0$ is standard atmospheric pressure and n is the reaction order. For e-$NO_3$RR, the reaction order is 1 and the reaction rate constants is calculated based on the equation as follows.

$$k = \frac{k_b T}{h}\exp\left(\frac{-E_a}{RT}\right) \quad (4)$$

## Supporting Information

Supporting Information is available from the Wiley Online Library or from the author.

## Acknowledgements

This project was supported by the grants from the City University of Hong Kong (Grant No. 9020005, 9610663, and 7020103), General Research Fund (Project no. CityU 9446008) from the Research Grants Council of Hong Kong SAR, China, ITF-RTH – Global STEM Professorship (9446008) and the Hong Kong Branch of National Precious Metals Material Engineering Research Center – ITC Fund. The authors acknowledge the National Key R&D Program of China (2021YFA1501101), Research Grant Council of Hong Kong (15304023), National Natural Science Foundation of China/Research Grant Council of Hong Kong Joint Research Scheme (N_PolyU502/21), National Natural Science Foundation of China/Research Grants Council of Hong Kong Collaborative Research Scheme (CRS_PolyU504/22), training plan for young backbone teacher of colleges and universities in Henan Province (2023GGJS143). X. Wang would also like to express his sincere appreciation to the Hong Kong Jockey Club for supporting his research under the JC STEM Lab of Electrocatalysis and Electrosynthesis (9228006).

## Conflict of Interest

The authors declare no conflict of interest.

## Author Contributions

Y.Z., M.S., and T.L. contributed equally to this work. Y.-P.Z. and T.-T.L. prepared the materials and performed all data processing and analysis. M.-Z.S. and B.H. conducted the simulations and theoretical analysis. L.-B.S., S.-H.H., Y.C., and X.W. provided experimental guidance. Y.-P.Z.,T.-T.L., and M.-Z.S. prepared the figures and wrote the manuscript. B.H. and X.W. reviewed and revised the manuscript and they also conceived and supervised the project.

## Data Availability Statement

The data that support the findings of this study are available from the corresponding author upon reasonable request.

## Keywords

ammonia synthesis, Cu Single atom, electrocatalysis, nitrate reduction, proton donor

Received: October 14, 2024
Revised: January 14, 2025
Published online: February 18, 2025

[1] V. Rosca, M. Duca, M. T. Groot, M. T. M. Koper, *Chem. Rev.* **2009**, *109*, 2209.
[2] G. Soloveichik, *Nat. Catal.* **2019**, *2*, 377.
[3] S. Han, H. Li, T. Li, F. Chen, R. Yang, Y. Yu, B. Zhang, *Nat. Catal.* **2023**, *6*, 402.
[4] Y. Wang, C. Wang, M. Li, Y. Yu, B. Zhang, *Chem. Soc. Rev.* **2021**, *50*, 6720.
[5] P. H. Van Langevelde, I. Katsounaros, M. T. M. Koper, *Joule* **2021**, *5*, 290.
[6] F. Y. Chen, Z. Y. Wu, S. Gupta, D. J. Rivera, S. V. Lambeets, S. Pecaut, J. Y. T. Kim, P. Zhu, Y. Z. Finfrock, D. M. Meira, G. King, G. Gao, W. Xu, D. A. Cullen, H. Zhou, Y. Han, D. E. Perea, C. L. Muhich, H. Wang, *Nat. Nanotechnol.* **2022**, *17*, 759.
[7] C. H. Christensen, T. Johannessen, R. Z. Sørensen, J. K. Nørskov, *Catal. Today* **2006**, *111*, 140.
[8] H. Iriawan, S. Z. Andersen, X. Zhang, B. M. Comer, J. Barrio, P. Chen, A. J. Medford, I. E. L. Stephens, I. Chorkendorff, Y. Shao-Horn, *Nat. Rev. Methods Primers* **2021**, *1*, 56.
[9] X. Fu, J. Pedersen, Y. Zhou, M. Saccoccio, S. Li, R. Sažinas, K. Li, S. Andersen, A. Xu, N. Deissler, J. Mygind, C. Wei, J. Kibsgaard, P. Vesborg, J. Nørskov, I. Chorkendorff, *Science* **2023**, *379*, 707.
[10] K. Zhang, A. Cao, L. H. Wandall, J. Vernieres, J. Kibsgaard, J. K. Nørskov, I. Chorkendorff, *Science* **2024**, *383*, 1357.
[11] K. Li, S. Z. Andersen, M. J. Statt, M. Saccoccio, V. J. Bukas, K. Krempl, R. Sažinas, J. B. Pedersen, V. Shadravan, Y. Zhou, D. Chakraborty, J. Kibsgaard, P. C. K. Vesborg, J. K. Nørskov, I. Chorkendorff, *Science* **2021**, *374*, 1593.
[12] S. Z. Andersen, V. Colic, S. Yang, J. A. Schwalbe, A. C. Nielander, J. M. McEnaney, K. Enemark-Rasmussen, J. G. Baker, A. R. Singh, B. A. Rohr, M. J. Statt, S. J. Blair, S. Mezzavilla, J. Kibsgaard, P. C. K. Vesborg, M. Cargnello, S. F. Bent, T. F. Jaramillo, I. E. L. Stephens, J. K. Norskov, I. Chorkendorff, *Nature* **2019**, *570*, 504.
[13] B. H. R. Suryanto, H.-L. Du, D. Wang, J. Chen, A. N. Simonov, D. R. MacFarlane, *Nat. Catal.* **2019**, *2*, 290.
[14] G.-F. Chen, Y. Yuan, H. Jiang, S.-Y. Ren, L.-X. Ding, L. Ma, T. Wu, J. Lu, H. Wang, *Nat. Energy* **2020**, *5*, 605.
[15] H. Xu, Y. Ma, J. Chen, W. X. Zhang, J. Yang, *Chem. Soc. Rev.* **2022**, *51*, 2710.
[16] M. Duca, M. T. M. Koper, *Energy Environ. Sci.* **2012**, *5*, 9726.
[17] M. P. Thorgersen, W. Lancaster, B. J. Vaccaro, F. L. Poole, A. Rocha, T. Mehlhorn, A. Pettenato, J. Ray, R. J. Waters, R. Melnyk, R. Chakraborty, T. Hazen, A. Deutschbauer, A. Arkin, M. Adams, *Appl. Environ. Microbiol.* **2015**, *81*, 4976.
[18] W. Zheng, L. Zhu, Z. Yan, Z. Lin, Z. Lei, Y. Zhang, H. Xu, Z. Dang, C. Wei, C. Feng, *Environ. Sci. Technol.* **2021**, *55*, 13231.
[19] H. Bagheri, A. Hajian, M. Rezaei, A. Shirzadmehr, *J. Hazard. Mater.* **2017**, *324*, 762.
[20] Y. H. Wang, A. Xu, Z. Y. Wang, L. S. Huang, J. Li, F. W. Li, J. Wicks, M. C. Luo, D. H. Nam, C. S. Tan, Y. Ding, J. W. Wu, Y. W. Lum, C. T. Din, D. Sinton, G. F. Zheng, E. H. Sargent, *J. Am. Chem. Soc.* **2020**, *142*, 5702.
[21] Z. X. Ge, T. J. Wang, Y. Ding, S. Bin Yin, F. M. Li, P. Chen, Y. Chen, *Adv. Energy Mater.* **2022**, *12*, 2103916.
[22] J. Ba, H. Dong, M. Odziomek, F. Lai, R. Wang, Y. Han, J. Shu, M. Antonietti, T. Liu, W. Yang, Z. Tian, *Adv. Mater.* **2024**, *36*, 2400396.
[23] G.-F. Chen, Y. Yuan, H. Jiang, S.-Y. Ren, L.-X. Ding, L. Ma, T. Wu, J. Lu, H. Wang, *Nat. Energy* **2020**, *5*, 605.
[24] Y.-Y. Lou, Q.-Z. Zheng, S.-Y. Zhou, J.-Y. Fang, O. Akdim, X.-Y. Ding, R. Oh, G.-S. Park, X. Huang, S.-G. Sun, *ACS Catal.* **2024**, *14*, 5098.
[25] J. Y. Fang, Q. Z. Zheng, Y. Y. Lou, K. M. Zhao, S. N. Hu, G. Li, O. Akdim, X. Y. Huang, S. G. Sun, *Nat. Commun.* **2022**, *13*, 7899.
[26] Z. Gu, Y. Zhang, X. Wei, Z. Duan, Q. Gong, K. Luo, *Adv. Mater.* **2023**, *35*, 2303107.
[27] J. Li, Y. Zhang, K. Kuruvinashetti, N. Kornienko, *Nat. Rev. Chem.* **2022**, *6*, 303.
[28] J. Li, H. Heidarpour, G. Gao, M. McKee, H. Bemana, Y. Zhang, C. Dinh, A. Seifitokaldani, N. Kornienko, *Nat. Synth.* **2024**, *3*, 809.
[29] Q. Gao, H. S. Pillai, Y. Huang, S. Liu, Q. Mu, X. Han, Z. Yan, H. Zhou, Q. He, H. Xin, H. Zhu, *Nat. Commun.* **2022**, *13*, 2338.
[30] J. Dai, Y. Zhu, Y. Chen, X. Wen, M. Long, X. Wu, Z. Hu, D. Guan, X. Wang, C. Zhou, *Nat. Commun.* **2022**, *13*, 1189.
[31] I. Ivanova, T. A. Kandiel, Y.-J. Cho, W. Choi, D. Bahnemann, *ACS Catal.* **2018**, *8*, 2313.
[32] J. Li, J. Hu, M. Zhang, W. Gou, S. Zhang, Z. Chen, Y. Qu, Y. Ma, *Nat. Commun.* **2021**, *12*, 3502.
[33] C. Xie, Z. Niu, D. Kim, M. Li, P. Yang, *Chem. Rev.* **2020**, *120*, 1184.
[34] D. Astruc, *Chem. Rev.* **2020**, *120*, 461.
[35] Y. Zuo, T. Li, N. Zhang, T. Jing, D. Rao, P. Schmuki, Š. Kment, R. Zbořil, Y. Chai, *ACS Nano* **2021**, *15*, 7790.
[36] Z. Peng, H. Yang, *Nano Today* **2009**, *4*, 143.
[37] Q. Wu, J. Xiong, Y. Zhang, X. Mei, Y. Wei, Z. Zhao, J. Liu, J. Li, *ACS Catal.* **2019**, *9*, 3700.
[38] H. R. Moser, B. Delley, W. D. Schneider, Y. Baer, *Phys. Rev. B* **1984**, *29*, 2943.
[39] R. D. Leapman, L. A. Grunes, P. L. Fejes, *Phys. Rev. B* **1982**, *26*, 614.
[40] Z. Bi, H. Zhang, X. Zhao, Y. Wang, F. Tan, S. Chen, L. Feng, Y. Zhou, X. Ma, Z. Su, X. Wang, T. Wågberg, G. Hu, *Energy Storage Mater.* **2023**, *54*, 313.
[41] J. Han, H. Bao, J.-Q. Wang, L. Zheng, S. Sun, Z. L. Wang, C. Sun, *Appl. Catal. B* **2021**, *280*, 119411.
[42] Y. Zuo, N. Antonatos, L. Děkanovský, J. Luxa, J. D. Elliott, D. Gianolio, J. Šturala, F. Guzzetta, S. Mourdikoudis, J. Regner, R. Málek, Z. Sofer, *ACS Catal.* **2023**, *13*, 2601.
[43] B. H. Lee, S. Park, M. Kim, A. K. Sinha, S. C. Lee, E. Jung, W. J. Chang, K. S. Lee, J. H. Kim, S. P. Cho, H. Kim, K. T. Nam, T. Hyeon, *Nat. Mater.* **2019**, *18*, 620.
[44] E. Murphy, Y. Liu, I. Matanovic, M. Ruscher, Y. Huang, A. Ly, S. Guo, W. Zang, X. Yan, A. Martini, J. Timoshenko, B. R. Cuenya, I. V. Zenyuk, X. Pan, E. D. Spoerke, P. Atanassov, *Nat. Commun.* **2023**, *14*, 4554.
[45] Q. Gao, B. Yao, H. S. Pillai, W. Zang, X. Han, Y. Liu, S.-W. Yu, Z. Yan, B. Min, S. Zhang, H. Zhou, L. Ma, H. Xin, Q. He, H. Zhu, *Nat. Synth.* **2023**, *2*, 624.
[46] W. Gao, K. Xie, J. Xie, X. Wang, H. Zhang, S. Chen, H. Wang, Z. Li, C. Li, *Adv. Mater.* **2023**, *35*, 2202952.
[47] J. Li, G. Zhan, J. Yang, F. Quan, C. Mao, Y. Liu, B. Wang, F. Lei, L. Li, A. W. M. Chan, L. Xu, Y. Shi, Y. Du, W. Hao, P. K. Wong, J. Wang, S.-X. Dou, L. Zhang, J. C. Yu, *J. Am. Chem. Soc.* **2020**, *142*, 7036.
[48] Y. Kim, J. Ko, M. Shim, J. Park, H.-H. Shin, Z. H. Kim, Y. Jung, H. R. Byon, *Chem. Sci.* **2024**, *15*, 2578.
[49] Y. Yeng, A. D. Handoko, Y. Du, S. Xi, B. S. Yeo, *ACS Catal.* **2016**, *6*, 2473.
[50] L. Cornaglia, J. Múnera, S. Irusta, E. Lombardo, *Appl. Catal. A* **2004**, *263*, 91.
[51] R. Lascola, L. Andrews, *J. Am. Chem. Soc.* **1987**, *109*, 4765.
[52] B. Ravela, M. Newville, *J. Synchrotron Rad* **2005**, *12*, 537.
[53] S. J. Clark, M. Segall, C. J. Pickard, P. J. Hasnip, M. Probert, K. Refson, M. C. Payne, *Z. Krist.-Cryst. Mater.* **2005**, *220*, 567.
[54] J.-P. Perdew, K. Burke, M. Ernzerhof, *Phys. Rev. Lett.* **1996**, *77*, 3865.
[55] P.-J. Hasnip, C.-J. Pickard, *Comput. Phys. Commun.* **2006**, *174*, 24.
[56] J. P. Perdew, J. A. Chevary, S. H. Vosko, K. A. Jackson, M. R. Pederson, D. J. Singh, C. Fiolhais, *Phys. Rev. B* **1993**, *46*, 6671.
[57] J.-D. Head, M.-C. Zerner, *Chem. Phys. Lett.* **1985**, *122*, 264.